Chinese Chemical Letters 37 (2026) 111481

Contents lists available at ScienceDirect

Chinese Chemical Letters

journal homepage: www.elsevier.com/locate/cclet

Multifunctional hydrogel embedded with Au–Cu nanoclusters for catalytic cascade therapy of infected diabetic wounds

Wenjing Zhang[a,b,1], Yu Chen[b,1], Kun Xie[b], Rachel A. Jun[c], Run Wang[d], Ning Wang[b], Yingwei Li[c,*], Yongbo Song[a,b,*]

[a] School of Pharmaceutical Sciences, Anhui Medical University, Hefei 230032, China
[b] School of Biomedical Engineering, Anhui Medical University, Hefei 230032, China
[c] Department of Chemistry, University of Hawai'i at Manoa, Honolulu, HI 96822, United States
[d] College & Hospital of Stomatology, Anhui Medical University, Hefei 230022, China

ARTICLE INFO

Article history:
Received 15 May 2025
Revised 15 June 2025
Accepted 17 June 2025
Available online 17 June 2025

Keywords:
Diabetic wound infection
Au–Cu nanoclusters
Injectable hydrogel
Catalytic cascade reactions
POD-like activity

ABSTRACT

Diabetic wound healing is hindered by multidrug-resistant bacteria, hyperglycemia, and oxidative stress, making bacterial control and microenvironment modulation crucial. However, an all-in-one strategy is still under development. We report a cascade catalytic hydrogel by incorporating quantum-sized Au–Cu bimetallic nanoclusters with dual enzyme-mimetic activities and glucose oxidase into a cross-linked matrix of oxidized chondroitin sulfate and carboxymethyl chitosan. Three objectives are achieved in this system: (1) Utilizing glucose oxidase to decrease blood glucose levels while generating H_2O_2. (2) Producing hydroxyl radicals *via* peroxidase-like activity of Au–Cu nanoclusters, while simultaneously functioning as a glutathione peroxidase-like to deplete GSH levels, thereby achieving effective antibacterial effect. (3) The Schiff base bonds (-CH=N-) within the hydrogel will responsively cleavage under slightly acidic environment of wound to release the oxidized chondroitin sulfate, which is benefit for down-regulating the levels of inflammatory factors (TNF-α and IL-6), ultimately achieving an anti-inflammatory effect. Comprehensive *in vitro* and *in vivo* evaluations, including antibacterial testing, biocompatibility, rapid hemostasis (within 7 min), and 16S rRNA gene sequencing, revealed that the hydrogel effectively restored microbial diversity and rectified the disrupted wound microenvironment. This work established the Au–Cu/GOx-integrated hydrogel as a promising therapeutic platform for treating infected diabetic wounds and highlights the potential of Au–Cu nanoclusters in clinical application.

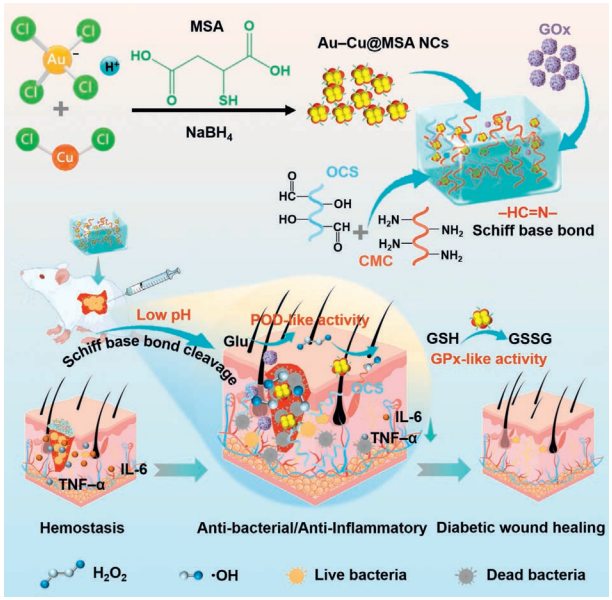
© 2026 Published by Elsevier B.V. on behalf of Chinese Chemical Society and Institute of Materia Medica, Chinese Academy of Medical Sciences.

Diabetes, a chronic metabolic disorder characterized by persistent hyperglycemia, presents major challenges for wound treatment due to glucose accumulation [1,2], bacterial colonization [3,4], impaired angiogenesis resulting in local hypoxia and elevated oxidative stress [5–7], all of which weaken antimicrobial defenses and contribute to ischemia and tissue necrosis [8–10]. To promote wound healing, a glucose cascade reaction has been developed—glucose oxidase (GOx)-like activity oxidizes glucose to produce hydrogen peroxide (H_2O_2) which further converts into highly reactive hydroxyl radicals ($^{\bullet}OH$) through peroxidase (POD)-like activity, facilitating glucose (Glu) depletion and bacterial eradication [11–13] while avoiding direct application of cytotoxic H_2O_2 and alleviating pH-associated limitations.

Given the pH and oxygen sensitivity of natural enzymes, multi-enzyme-mimicking nanozymes have been engineered to address the hypoxic microenvironment in diabetic wounds, in which Au-based nanomaterials stand out for their biocompatibility, low cytotoxicity, and broad antimicrobial efficacy [14–18]. Quantum-sized (<2 nm) metal nanoclusters (NCs) have emerged as promising nanomaterials for various bio-applications due to their molecular-like properties [19–24]. In wound infection management, NCs offer distinct therapeutic advantages over conventional nanoparticles (NPs), including energy-independent translocation across bacterial membranes [25], and a high density of surface active sites for modulating intercellular processes [26,27]. For example, 6-mercaptohexanoic acid (MHA) stabilized Au_{25} NCs demonstrate potent antibacterial efficacy against Gram-negative bacteria [28], while glutathione-protected Ag NCs conjugated with daptomycin lead to synergistic enhancement of antibacterial activity [29]. Direct application of NCs to wound sites, however, makes them susceptible to aggregation and/or degradation upon exposure

* Corresponding authors.
E-mail addresses: yingweil@hawaii.edu (Y. Li), ybsong860@ahmu.edu.cn (Y. Song).
[1] These authors contributed equally to this work.

https://doi.org/10.1016/j.cclet.2025.111481
1001-8417/© 2026 Published by Elsevier B.V. on behalf of Chinese Chemical Society and Institute of Materia Medica, Chinese Academy of Medical Sciences.



Scheme 1. Schematic illustration of Au–Cu/GOx/CMC–OCS hydrogel and its application for the treatment of infected diabetic wound.

to air, thereby compromising their efficacy and safety [30]. Among the rare reported cases, $Au_{25}(MHA)_{18}$ NCs have been incorporated into injectable hydrogels *via* hydrogen bonding [31], and hydrogels also offers controlled release of Ag NCs to enhance antibacterial efficacy [32]. Moreover, alloying offers precise tailoring of NC size, geometry, electronic structure and surface chemistry [23,33], although the antibacterial properties of bimetallic NCs remain largely underexplored.

In this work, we present a multi-functional hydrogel, crosslinked from oxidized chondroitin sulfate (OCS) and carboxymethyl chitosan (CMC), and embedded with water-soluble Au–Cu NCs and GOx (Scheme 1). The mercaptosuccinic acid (MSA)-stabilized Au–Cu NCs exhibit dual enzyme-mimetic (POD-like and glutathione peroxidase like (GPx-like)) activities, enabling synergistic antibacterial effects *via* a cascade catalytic therapy and enhanced wound healing—capabilities absent in monometallic Au or Cu NCs. Additionally, the Schiff base bonds within the Au–Cu/GOx/CMC–OCS hydrogel can be disrupted in response to the low pH of the wound environment. This disruption allows the release of OCS, which effectively reduces the levels of inflammatory factors (TNF-α and IL-6) at the wound site. A comprehensive evaluation both *in vitro* and *in vivo* confirmed the hydrogel's superior antibacterial efficacy, biocompatibility, and ability to accelerate tissue regeneration and restore skin microecology. The work presents an unprecedented integration of water-soluble Au–Cu NC in a multifunctional hydrogel, achieving synergistic antibacterial, anti-inflammatory, and regenerative effects and offering a powerful platform for effective diabetic wound treatment.

Au–Cu NCs stabilized by mercaptosuccinic acid were prepared by a direct method adapted from reported procedures [34], using a molar ratio of Au:Cu = 2:2.6. The UV–vis spectrum of the as-synthesized Au–Cu@MSA NCs displayed an almost featureless profile, with only a weak absorption shoulder near 380 nm (Fig. 1a), which is distinct from the pronounced plasmonic resonance peaks observed in larger (8–13 nm) Au–Cu NPs [35]. The zeta potential of the bimetallic NCs was around –24 mV at neutral pH (Fig. S1 in Supporting information), close to that of well-studied water soluble Au_{25} NCs [36], indicating good stability. Inductively coupled plasma mass spectrometry analysis suggested an atomic ratio of Au:Cu = 1:2.42 (Fig. S2 in Supporting information). High-resolution transmission electron microscopy (HRTEM) images revealed that Au–Cu@MSA NCs were uniformly spherical with an average diameter of ~1.8 nm (Figs. 1b and c). And the elemental mapping further confirmed the homogeneous distribution of Au, Cu and S within the Au–Cu@MSA NCs (Fig. 1d). For comparison, the monometallic Au@MSA and Cu@MSA NCs were synthesized in the same way (Figs. S3 and S4 in Supporting information).

The valence states of Au and Cu in the Au–Cu NCs were further investigated by X-ray photoelectron spectroscopy (XPS). The Au $4f_{7/2}$ binding energy was observed at 84.39 eV (Fig. 1e), while the Cu $2p_{3/2}$ peak appeared at 932.55 eV (Fig. 1f), along with a Cu LMM Auger peak at 570.0 eV (Fig. S5 in Supporting information). The XPS results, together with HRTEM imaging, confirm the formation of Au–Cu@MSA NCs, in which Cu atoms, exhibiting predominant Cu^{I} character, are likely enriched on the surface, while Au atoms are preferentially located in the core, consistent with previously reported Au–Cu NCs of atomic precision [37–39].

The successful generation of reactive oxygen species (ROS), particularly hydroxyl radicals (·OH), in the cascade reaction was demonstrated through two chromogenic substates (Fig. 2a): (1) Colorless 3,3′,5,5′-tetramethylbenzidine (TMB) was oxidized to its blue product (ox-TMB) with a characteristic absorbance at 652 nm, and (2) colorless *o*-phenylenediamine (OPD) was oxidized to its yellow dimeric product (ox-OPD), showing a strong absorption at 420 nm [40]. Among all tested groups, the presence of

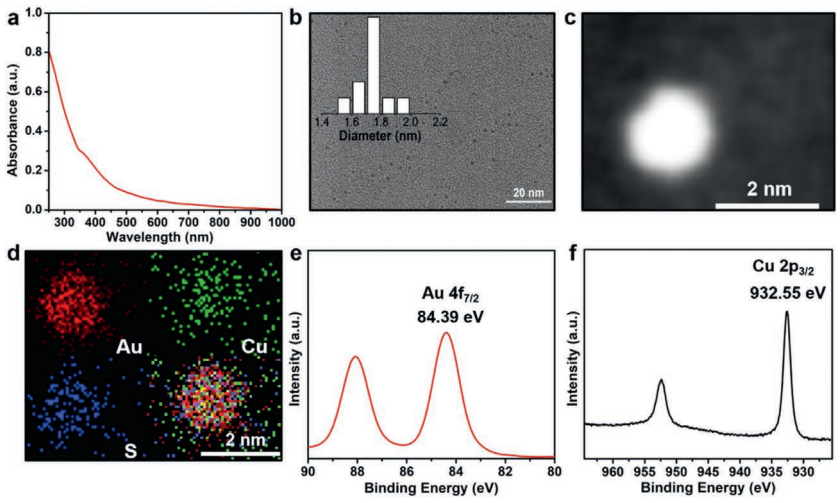


Fig. 1. (a) UV–vis spectrum, (b, c) HRTEM images, (d) elemental mapping and (e, f) XPS spectra of Au–Cu@MSA NCs.

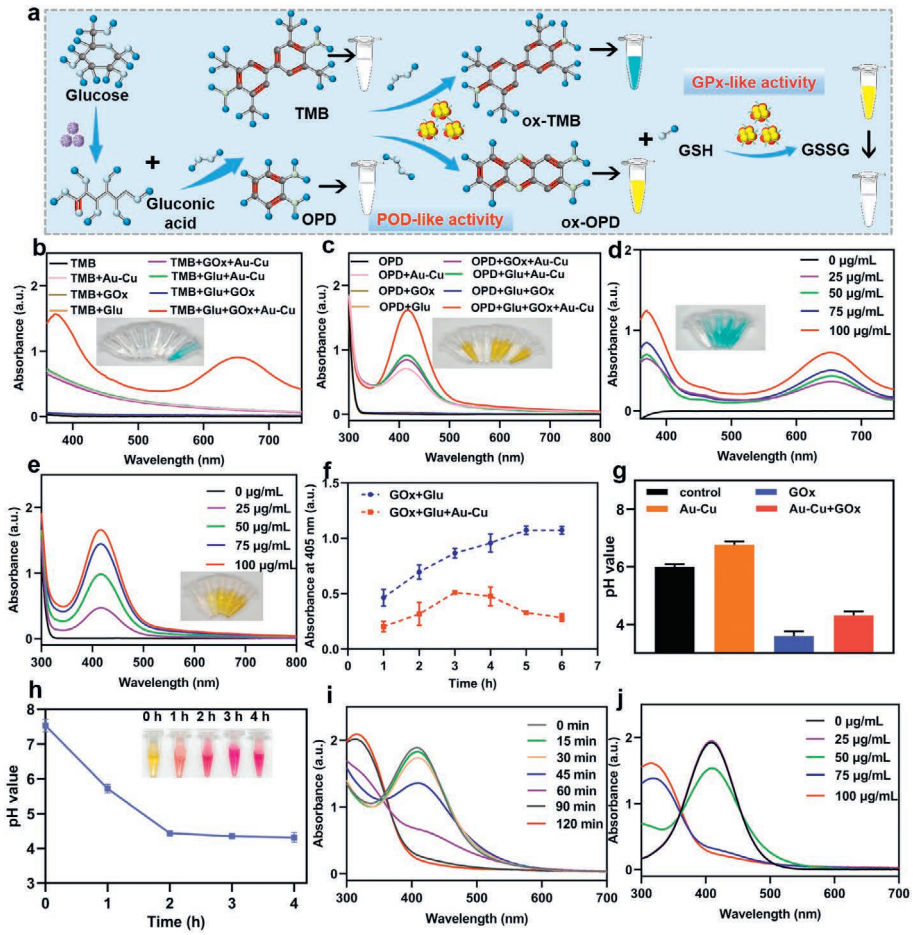


Fig. 2. (a) Schematic diagram of Au−Cu@MSA NCs with POD-like and GPx-like activities. UV−vis spectra of (b) TMB oxidation and (c) OPD oxidation under different conditions (Inset: the corresponding pictures). UV−vis spectra of (d) TMB+Glu+GOx and (e) OPD+Glu+GOx treated with different concentrations of Au−Cu@MSA NCs. (f) Time-dependent H_2O_2 generation catalyzed by GOx+Glu or Glu+GOx+Au−Cu@MSA. (g) pH values of glucose solutions (10 mmol/L) after incubating under different conditions for 4 h. (h) Time-dependent pH variation of a 10 mmol/L glucose solution catalyzed by GOx+Au−Cu@MSA NCs. Inset: the corresponding photographs. (i) Time-dependent GSH depletion catalyzed by Au−Cu@MSA NCs using DTNB as probe (0.1 mmol/L). (j) GSH depletion of Au−Cu@MSA NCs at different concentrations using the DTNB probe.

Au−Cu@MSA NCs was essential to facilitate substantial ox-TMB formation (Fig. 2b) [16,41], confirming that the bimetallic NCs exhibit intrinsic POD-like activity and efficiently convert H_2O_2 (produced during glucose oxidation by GOx) into •OH.

In contrast, neglectable color change was observed with Au@MSA NCs, and Cu@MSA NCs generated a much-reduced response (Fig. S6a in Supporting information). Additionally, bimetallic NCs synthesized using glutathione (GSH) ligands (Au−Cu@SG NCs) as well as $Au_{25}(SG)_{18}$ NCs [42], also oxidize TMB but with lower efficiency than Au−Cu@MSA NCs (Fig. S6b in Supporting information). In the other scenario, Au−Cu@MSA NCs along were capable of oxidizing OPD without the addition of glucose or GOx (Fig. 2c). In contrast, Cu@MSA NCs showed much weaker ox-OPD generation, while Au@MSA NCs led to undesired polymerization of OPD [43], a phenomenon also observed for Au_{25}@SG NCs (Fig. S7 in Supporting information). The following two points may provide a plausible explanation for this phenomenon: (1) The differences in atomic radii and electronic structures between Au and Cu atoms enable the formation of new active sites *via* charge redistribution of Au−Cu@MSA NCs [44]; (2) Compared with monometallic Au@MSA and Cu@MSA NCs, alloying will endow the Au−Cu@MSA NCs with unique atomic arrangements and surface coordination environments, thereby enhancing the generation of reactive oxygen species [45]. Moreover, in the presence of glucose and GOx, the POD-like activity of Au−Cu@MSA NCs increases as its concentration increases from 0 to 100 μg/mL (Figs. 2d and e).

GSH, a key intercellular antioxidant, can scavenge ROS in bacteria and thereby diminish the antibacterial efficacy of wound-healing materials [46–48]. Nanozymes with glutathione peroxidase-like (GPx) activity offer a strategy to mediate GSH depletion and enhance therapeutic outcomes [49–51]. To assess the GPx-like activity of the NCs, 5,5′-dithiobis(2-nitrobenzoic acid) (DTNB) was used as a thiol-specific probe for GSH. Upon incubation with Au−Cu@MSA NCs, the characteristic absorbance peak of 2-nitro-5-mercapto-benzoic acid (TNB) disappeared, in contrast to the minimal changes observed with monometallic Au@MSA NCs, Cu@MSA NCs (Fig. S8a in Supporting information), and Au_{25}@SG NCs (Fig. S8b in Supporting information), indicating that GSH depletion is specific to the bimetallic Au−Cu NCs, regardless of whether they are stabilized by MSA or SG.

The concentration of H_2O_2 was monitored by measuring the absorbance at 405 nm using $Ti(SO_4)_2$ as the colorimetric indicator. Continuous catalysis of glucose by GOx led to H_2O_2 accumulation, reaching equilibrium within 5 h. Upon incorporation of Au−Cu@MSA NCs, a rapid reduction in H_2O_2 concentration was observed, particularly after 3 h (Fig. 2f), indicating active ROS conversion and demonstrating that the cascaded reaction system provided an appropriate pH for triggering the subsequent POD-like activity [52]. As shown in Fig. 2g, when catalyzed by GOx and Au−Cu@MSA NCs+GOx, the pH value of the glucose solution was significantly reduced to a final pH range of 3–5, which provided the essential pH conditions for activating the subsequent POD-like

activity. Besides, under the catalysis of Au−Cu@MSA+GOx, the pH stabilized around 4.5 after 2 h (Fig. 2h) [53]. The GPx-like activity of Au−Cu@MSA NCs was further shown to depend on both reaction time and NC concentration (Figs. 2i and j), with nearly complete GSH depletion achieved at 90 min and a minimum effective concentration threshold of 75 μg/mL.

Hydrogels incorporated with nanozymes have demonstrated multifunction in enhanced diabetic wound healing [54,55]. An injectable hydrogel was synthesized *via* the crosslinking of oxidized chondroitin sulfate (OCS) and carboxymethyl chitosan (CMC) [56], with Au−Cu@MSA NCs and GOx incorporated into the matrix (Fig. S9 in Supporting information). The formation of the OCS−CMC hydrogels was confirmed by Fourier transform infrared (FTIR) spectra (Fig. S10 in Supporting information), and HRTEM elemental mapping demonstrated the homogeneous distribution of Au and Cu atoms within the Au−Cu/GOx/CMC−OCS hydrogel, without altering its morphology (Fig. S11 in Supporting information).

The rheological properties—critical for clinical hydrogel applications—were evaluated to assess viscoelastic behavior. Across an angular frequency range of 0.1–100 rad/s, the storage modulus (*G*') exceeded the loss modulus (*G*") for both the control (CMC−OCS hydrogel) and the Au−Cu/GOx/CMC−OCS hydrogel (Fig. S12 in Supporting information), confirming successful hydrogel formation. Strain-sweep tests at a fixed angular frequency of 10 rad/s revealed broad linear viscoelastic regions, with strain tolerance of approximately 460 % (Fig. S13 in Supporting information). Smooth extrusion upon injection further demonstrated favorable injectability, attributed to Schiff base-mediated network formation (Fig. S14 in Supporting information). And exhibited shear-thinning behavior—characterized by decreasing viscosity with increasing shear rate—supporting its excellent injectability (Fig. S15 in Supporting information).

Self-healing properties were demonstrated both visually (Fig. S14 in Supporting information) and through dynamic rheological cycling. At low strain (10 %), the hydrogel remained in a solid state (*G*' > *G*"), while application of high strain (600 %) disrupted the network, shifting it to a liquid-like state. Upon restoring strain to 10 %, *G*' and *G*" rapidly recovered, reflecting the reversible Schiff base linkages. Under extreme deformation (600 % strain), *G*' again fell below *G*", confirming viscosity-dominated behavior (Fig. S16 in Supporting information). The hydrogel also adheres well to various substrates (Fig. S17 in Supporting information).

The swelling properties of freeze-dried CMC−OCS and Au−Cu/GOx/CMC−OCS hydrogels were evaluated at 37 °C. Both hydrogels demonstrated rapid expansion within the first 30 min, reaching equilibrium swelling of approximately 2700 % within 1 h (Fig. S18a in Supporting information), indicating that the Au−Cu/GOx-loaded hydrogel is capable of efficiently absorbing substantial amounts of wound exudate, and thus, promoting the wound healing process [57,58]. *In vitro* degradation studies revealed that the Au−Cu/GOx/CMC−OCS hydrogel retained ~35 % of its original mass after 3 days of incubation in phosphate-buffered saline (PBS, pH 4). Notably, degradation proceeded more slowly in PBS at pH 7.4 (Fig. S18b in Supporting information), likely due to acid-sensitive cleavage of Schiff base linkages within the hydrogel network.

Bacterial infection significantly impedes the healing of diabetic wounds, highlighting the urgent need for effective antibacterial wound dressings in clinical settings. We showed that Au−Cu@MSA NCs, in conjunction with GOx, generated substantial quantities of ·OH, contributing to enhanced antibacterial activity. A representative methicillin-resistant *Staphylococcus aureus* (MRSA) strain was selected to investigate the antibacterial efficacy of Au−Cu@MSA NCs and Au−Cu/GOx/CMC−OCS hydrogels *in vitro*. Antibacterial efficacy was evaluated using the spread plate method [59–61]. Increasing concentrations of Au–Cu@MSA NCs led to progressively

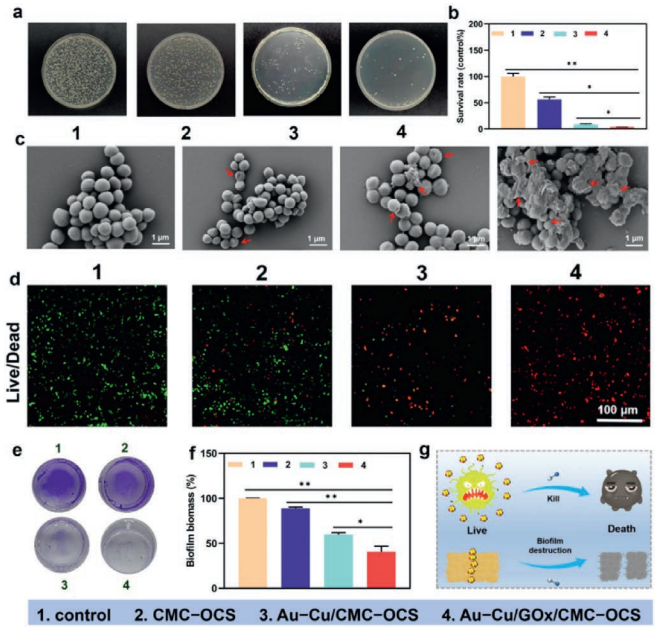


Fig. 3. *In vitro* antibacterial evaluation of control (PBS), CMC−OCS, Au−Cu/CMC−OCS and Au−Cu/GOx/CMC−OCS hydrogels. (a) Photographs of survival MRSA colonies following treatment. (b) MRSA survival rate. (c) SEM images of MRSA following treatment. (d) Live (SYTO 9)/dead (PI) fluorescence staining images of MRSA. (e) Photographs of crystal violet stained MRSA biofilms. (f) Quantitative analysis of relative MRSA biofilm biomass. (g) Schematic illustration of the antibacterial mechanism. Data are presented as mean ± SD ($n = 3$). $^{*}P < 0.05$, $^{**}P < 0.01$.

greater MRSA inhibition, with complete eradication achieved at 100 μg/mL in the presence of GOx (Figs. S19 and S20 in Supporting information).

Among the hydrogels tested, although Au−Cu/CMC−OCS hydrogel demonstrated antibacterial effects, the hydrogel incorporating both Au−Cu@MSA NCs and GOx (Au−Cu/GOx/CMC−OCS) showed the most pronounced activity (Fig. 3a). Compared to CMC−OCS (56.36 %), the MRSA survival rates after treatment with Au−Cu/CMC−OCS hydrogels dropped to 8.62 %, which further decreased to just 3.78 % when exposed to Au−Cu/GOx/CMC−OCS hydrogel (Fig. 3b). Scanning electron microscopy (SEM) imaging further confirmed bacteria membrane damage induced by the hydrogels. While the control group (PBS) showed intact MRSA morphology, bacterial cells treated with CMC−OCS, and Au−Cu/CMC−OCS hydrogels exhibited some degrees of membrane damage. Notably, MRSA treated with the Au–Cu/GOx/CMC–OCS hydrogel displayed severe shrinkage and membrane cracking (Fig. 3c). Consistent results were observed in live/dead fluorescence assays, where the majority of MRSA treated with the Au−Cu/GOx/CMC−OCS hydrogel died, in contrast to high bacterial viability in the other treatment groups (Fig. 3d and Fig. S21 in Supporting information).

The biofilm removal capability of the Au−Cu/GOx/CMC−OCS hydrogel in a glucose-containing environment was further evaluated using crystal violet staining. The hydrogel showed strong antibacterial activity through the destruction of bacterial biofilms (Figs. 3e and f), indicating that the Au−Cu/GOx/CMC−OCS hydrogel effectively released Au–Cu NCs and GOx, which generated large amounts of •OH in the presence of glucose, thereby killing MRSA (Fig. 3g).

The *in vitro* cytocompatibility of Au−Cu/GOx/CMC−OCS hydrogel was assessed using mouse fibroblast cell line (L929) and Human keratinocytes (HaCaT) *via* the methylthiazolyldiphenyltetrazolium bromide (MTT) assay. After 24 h of incubation with hy-

drogel containing 25 μg/mL Au−Cu@MSA NCs, both cell type exhibited excellent viability; however, increased cytotoxicity was observed at higher concentrations (100 μg/mL) (Fig. S22 in Supporting information). To further evaluate therapeutic potential, the hydrogels were applied in the context of MRSA infections. Cell viability remained nearly 100 % for both L929 and HaCaT cells when treated with CMC−OCS, Au−Cu/CMC−OCS, and Au−Cu/GOx/CMC−OCS hydrogels. In contrast, the GOx/CMC−OCS hydrogel showed significant cytotoxicity towards both cells (Fig. S23 in Supporting information). These results indicate that the Au−Cu/GOx/CMC−OCS hydrogel maintains excellent biocompatibility while exhibiting dual POD-like and GPx-like activities that effectively converted produced H_2O_2 to generate ROS. Furthermore, the excellent biological safety of the Au−Cu/GOx/CMC−OCS hydrogel was verified by a hemolysis test in which the hemolysis rates were below 5 % (Fig. S24 in Supporting information).

A scratch test was conducted to evaluate the influence of Au−Cu@MSA NCs and GOx on L929 cell migration. After 24 h treatment, enhanced wound closure was observed in groups treated with CMC−OCS, Au−Cu/CMC−OCS, and Au−Cu/GOx/CMC−OCS hydrogels, compared to the PBS control. Significantly, the Au−Cu/GOx/CMC−OCS hydrogel demonstrated the most pronounced effect on cell migration (Fig. S25 in Supporting information). This enhancement is attributed to the sustained release of Au−Cu@MSA NCs and GOx from the hydrogel, which synergistically exert antibacterial effects *via* a cascade catalytic reaction. Additionally, degradation of the CMC−OCS network and the bioactivity of OCS contributed to anti-inflammatory effects, thereby promoting wound closure. These results highlighted the good potentials of the Au−Cu/GOx/CMC−OCS hydrogel as an advanced therapeutic strategy for diabetic wound healing.

Hemostasis performance of Au−Cu/GOx/CMC−OCS hydrogel was then studied to reveal the initial phase of wound healing in different bleeding environments [62], and models of liver hemorrhage and tail-cutting hemorrhage were established in mice (Figs. S26a and b in Supporting information). In the absence of hydrogel treatment, the liver and tail of the control mice continued to bleed. In contrast, the application of Au−Cu/GOx/CMC−OCS hydrogel at the bleeding sites resulted in a much-reduced bleeding volume (Figs. S27a and b in Supporting information), aligning with the high swelling capacity of Au−Cu/GOx/CMC−OCS hydrogel, which promoted the rapid absorption of wound exudate.

The therapeutic efficacy of the Au−Cu/CMC−OCS hydrogel for treating MRSA-infected diabetic wounds was evaluated in a streptozotocin (STZ)-induced diabetic mouse model (Fig. 4a). The animal study was approved by the Animal Ethics Committee of Anhui Medical University (approval No. LLSC 20242365). All experimental procedures involving animals were conducted in strict accordance with the guidelines of the Committee on the Ethics of Animal Experiments of Anhui Medical University. Mice were randomly assigned to four groups: PBS (control), CMC−OCS hydrogel, Au−Cu/CMC−OCS hydrogel, and Au−Cu/GOx/CMC−OCS hydrogel. MRSA-infected wounds were created, and wound areas were monitored on days 1, 4, 8, and 12 across different groups. The Au−Cu/GOx/CMC−OCS hydrogel group demonstrated significantly accelerated wound healing with nearly complete closure by day 12 and only 4.18 % residual wound area (Figs. 4b-d). In contrast, wound areas in the CMC−OCS and Au−Cu/CMC−OCS groups remained at 22.86 % and 16.87 %, respectively, indicating slower healing. On day 12, MRSA colonies were isolated from wound tissues for bacterial load analysis, where the Au−Cu/GOx/CMC−OCS hydrogel-treated group exhibited markedly reduced bacterial counts, confirming superior *in vivo* antibacterial efficacy (Figs. 4e and f). Additionally, body weight remained stable across all groups during treatment, supporting the hydrogel's excellent systemic biocompatibility (Fig. 4g).

The wound healing process in diabetic mice was studied by evaluating re-epithelization and granulation tissue formation [63]. On day 12, histological analyses were performed using Hematoxylin and Eosin (H&E) staining and Masson's trichrome staining across all treatment groups (Fig. S28 in Supporting information). Wounds treated with the Au−Cu/GOx/CMC−OCS hydrogel exhibited well-developed epithelial layers, thick granulation tissue, and limited presence of hair follicles (Figs. S28a and S29a in Sup-

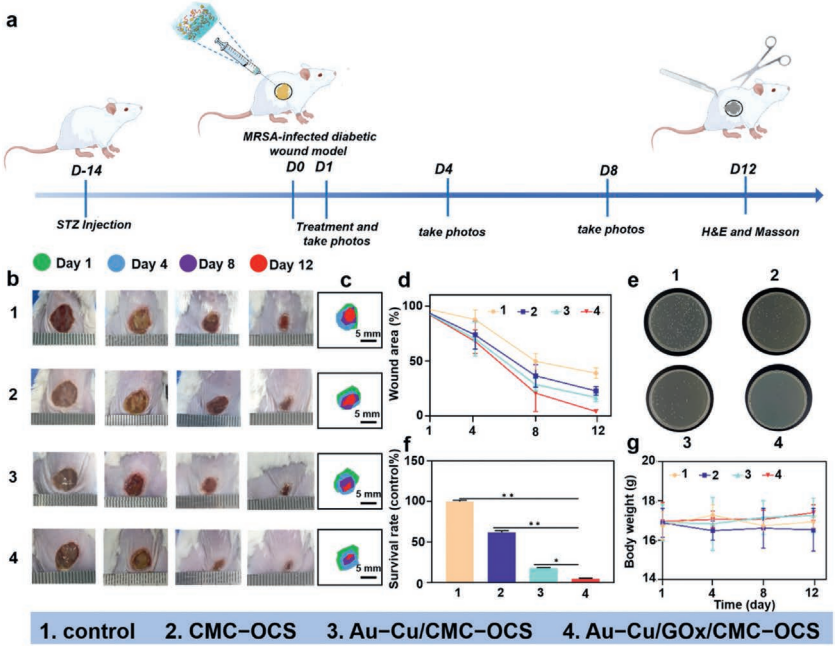


Fig. 4. *In vivo* therapeutic effects of hydrogels on MRSA-infected diabetic wounds. (a) Schematic illustration of the diabetic wound infection model and treatment strategy. (b) Representative wound photographs captured at designated time points. (c) Overlay images of the wound healing process during the treatment. (d) Percentage of wound area remaining over time for each treatment group ($n = 4$). (e) Photographs of surviving bacteria colonies isolated from wound tissues on day 12. (f) *In vivo* bacterial survival rate across different groups on day 12 ($n = 3$). (g) Body weight measurements of mice in each treatment group recorded at designated time points ($n = 4$), $^{*}P < 0.05$, $^{**}P < 0.01$.

porting information). Masson's staining revealed much-enhanced collagen deposition in the Au−Cu/GOx-loaded hydrogel group compared to other treatments (Figs. S28a and S29b in Supporting information). In diabetic wound sites, sustained hyperglycemia can stimulate excessive ROS production, aggravating cellular damage, prolonging inflammation, and impairing tissue regeneration [64], which is often accompanied by elevated level of pro-inflammatory cytokines, further disrupting the healing process [65,66]. To assess the hydrogel's immunomodulatory effect, immunohistochemical staining was conducted for tumor necrosis factor-α (TNF-α) and interleukin-6 (IL-6), both of which showed significantly reduced expression in the Au−Cu/GOx/CMC−OCS group (Figs. S28b, S30a and b in Supporting information). Furthermore, angiogenesis was evaluated by staining for CD31 and vascular endothelial growth factor (VEGF), two key markers of neovascularization during wound repair [67]. Both markers were upregulated in the Au−Cu/GOx/CMC−OCS-treated wounds (Figs. S28b, S30c and d in Supporting information), indicating enhanced vascularization.

The biocompatibility of the Au−Cu/GOx/CMC−OCS hydrogel was further validated *in vivo* through histological and biochemical analyses. H&E staining was performed on major organs, including heart, liver, spleen, lung, and kidney, collected from mice in different treatment groups on day 12 of wound healing. No obvious histopathological abnormalities were detected in any group (Fig. S31a in Supporting information), confirming the absence of systemic toxicity. Moreover, serum biochemical markers, including γ-GT, AST/GOT, ALT/GPT, BUN, CRE and AKP, remained within normal ranges and showed no significant differences compared to the PBS control group (Fig. S31b in Supporting information). These findings collectively indicate that the Au−Cu/GOx/CMC−OCS hydrogel is a safe, biocompatible, and low-toxicity therapeutic candidate for the treatment of infected diabetic wounds.

Skin microflora plays a vital role in maintaining the integrity of the skin barrier, contributing to the prevention of pathogenic colonization and regulation of local immune responses [68,69]. In diabetic wounds, previous studies have reported significant disruption in microbial homeostasis, including a notable reduction in microbial diversity [70]. To investigate whether the Au−Cu/GOx/CMC−OCS hydrogel could help restore the skin microecology in diabetic wounds, 16S rRNA sequencing was performed. Venn diagram analysis (Fig. 5a) revealed a total of 2020 operational taxonomic units (OTUs) identified across all groups, including 592 core OTUs shared among them. The number of OTUs to each group was as follows: control (PBS), 971; CMC−OCS hydrogel, 1175; Au−Cu/CMC−OCS hydrogel, 1176; Au−Cu/GOx/CMC−OCS hydrogel, 1212; and healthy (untreated) mice, 1498.

Metabolic disorders such as diabetes are commonly associated with a reduction in microbial diversity, and thus, diabetic model mice exhibited significantly lower skin microbial diversity compared to healthy controls. Notably, treatment with the Au−Cu/GOx/CMC−OCS hydrogel substantially enhanced microbial diversity (high Shannon index) in diabetic wounds (Fig. S32a in Supporting information). Although no significant differences were observed in microbial richness across treatment groups, as indicated by the Chao index (Fig. S32b in Supporting information), the hydrogel demonstrated a clear effect on microbial community structure.

To further evaluate microbial composition, β-diversity and principal coordinate analysis (PCoA) based on Binary-Chisq distance were conducted. The results demonstrated distinct clustering of skin microbiota among all groups, with a pronounced separation between the diabetic control and healthy mice, reflecting substantial alterations in microbial composition (Fig. 5b). Notably, microbial profiles from the Au−Cu/GOx/CMC−OCS hydrogel group were closely aligned with those of healthy mice, as confirmed by both

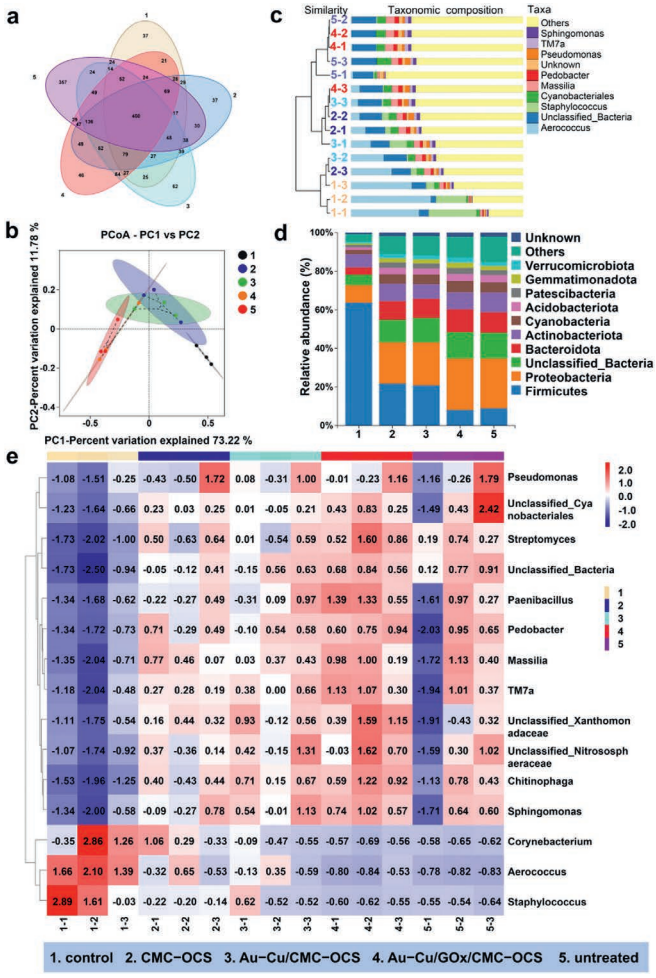


Fig. 5. Skin microbiota analysis during wound healing. (a) Venn diagram illustrating shared and unique OTUs among treatment groups. (b) PCoA plots of differences in microbial community composition. (c) UPGMA hierarchical clustering tree with accompanying histogram showing relative bacterial abundance. (d) Skin microbiota composition at the phylum level. (e) Skin microbiota composition at the genus level.

unweighted pair group method with arithmetic mean (UPGMA) hierarchical clustering and bacterial abundance histograms. The branch distance between the Au−Cu/GOx/CMC−OCS and healthy groups was significantly shorter than for other treatment groups, indicating a greater similarity in microbial community structure. This restorative effect suggests that the Au−Cu/GOx/CMC−OCS hydrogel effectively rebalance the dysbiotic wound microbiota. Unlike conventional antibiotics, which often cause broad−spectrum microbial depletion and dysbiosis, this hydrogel promotes restoration of the native microbiome, suppressing pathogenic overgrowth while preserving microbial diversity—an essential factor for optimal tissue regeneration and wound healing (Fig. 5c). Overall, CMC−OCS, Au−Cu/CMC−OCS, and Au−Cu/GOx/CMC−OCS hydrogels each contributed to partial restoration of the disrupted skin microecology in diabetic wounds, with the Au−Cu/GOx/CMC−OCS hydrogel demonstrating the most pronounced and comprehensive improvement.

At the phylum level, *Firmicutes* predominated in the diabetic control group, while *Proteobacteria* and *Bacteroidota* were dominant in the healthy group (Fig. 5d). Notably, the skin microbial profile of the Au−Cu/GOx/CMC−OCS hydrogel-treated group closely resembled that of the healthy group, suggesting effective restoration of skin microbial balance. At the genus level, treatment with the Au−Cu/GOx/CMC−OCS hydrogel significantly enhanced

the relative abundance of beneficial commensal bacteria (Fig. 5e), such as *Streptomyces* (Fig. S33a in Supporting information) and *Chitinophaga* (Fig. S33b in Supporting information). *Streptomyces* is recognized for its ability to produce antimicrobial compounds that protect the host against pathogen invasion [71]. Specifically, *Streptomyces* sp. APmarine042 has been reported to secrete anti-aging bioactive metabolites [72], and its abundance was restored to near-normal levels following Au−Cu/GOx/CMC−OCS hydrogel treatment. While the functional role of *Chitinophaga* in the skin remained unclear, prior studies suggest that it may generate various metabolites with antimicrobial activity when co-cultured with other symbiotic skin bacteria [73].

Furthermore, a significant decrease was observed in the relative abundance of opportunistic pathogens such as *Aerococcus*, *Staphylococcus*, and *Corynebacterium* (Figs. S33c-e in Supporting information), bacteria associated with infections [74–78], following treatment with the Au−Cu/GOx/CMC−OCS hydrogel. The suppression of these infection-associated genera underscores the hydrogel's potent microbiota-modulating effect, which is likely contributes to its accelerated wound healing efficacy in diabetic mice and highlights its potential for further clinical investigation.

In summary, an injectable CMC−OCS hydrogel incorporating quantum-sized Au−Cu NCs as dual-functional nanozymes has been developed as an integral solution to combat bacterial infections and inflammation, reshaping the pathological microenvironment for improved diabetic wound healing. Specifically, an effective cascade catalytic system is established through the synergistic activity of Au−Cu NCs and GOx, enabling rapid MRSA eradication and biofilm disruption, while the release of chondroitin sulfate from the hydrogel provides anti-inflammation. Comprehensive *in vitro* and *in vivo* evaluations confirmed the Au−Cu/GOx/CMC−OCS hydrogel's potent multifunctional capabilities and excellent biocompatibility, demonstrating its promise as a safe and effective therapeutic strategy that promotes collagen deposition, enhances angiogenesis, and restores microbial homeostasis, achieving near-complete re-epithelialization and organized tissue regeneration.

CRediT authorship contribution statement

Wenjing Zhang: Writing – review & editing, Writing – original draft, Resources, Investigation, Data curation. **Yu Chen:** Writing – review & editing, Writing – original draft, Resources, Data curation. **Kun Xie:** Resources, Data curation. **Rachel A. Jun:** Writing – original draft. **Run Wang:** Writing – original draft, Investigation. **Ning Wang:** Data curation. **Yingwei Li:** Writing – review & editing, Writing – original draft, Supervision. **Yongbo Song:** Writing – review & editing, Writing – original draft, Supervision, Project administration, Conceptualization.

Declaration of competing interest

The authors declare that they have no known competing financial interests or personal relationships that could have appeared to influence the work reported in this paper.

Acknowledgments

This work was financially supported by the Natural Science Foundation of China (Nos. 22171007 and 21801001), Anhui Provincial Natural Science Foundation (No. 2308085Y08), and Scientific Research (Nos. XJ2020026 and 2023xkj054) from Anhui Medical University.

Supplementary materials

Supplementary material associated with this article can be found, in the online version, at doi:10.1016/j.cclet.2025.111481.

References

[1] Y. Liang, M. Li, Y. Yang, et al., ACS Nano 16 (2022) 3194–3207.
[2] C.C. Lan, C.S. Wu, S.M. Huang, et al., Diabetes 62 (2013) 2530–2538.
[3] F.Y. Gao, Y. Wu, L. Yang, et al., Chin. Chem. Lett. 36 (2025) 109917.
[4] Y. Zhao, Z. Li, S. Song, et al., Adv. Funct. Mater. 29 (2019) 1901474.
[5] S.B. Catrina, X. Zheng, Diabetologia 64 (2021) 709–716.
[6] B. Hu, M. Gao, K.O. Boakye-Yiadom, et al., Bioact. Mater. 6 (2021) 4592–4606.
[7] H. Zhao, J. Huang, Y. Li, et al., Biomaterials 258 (2020) 120286.
[8] Q. Li, M. Dong, Q. Han, et al., J. Control. Release 365 (2024) 905–918.
[9] S.C. Hu, C.E. Lan, J. Dermatol. Sci. 84 (2016) 121–127.
[10] L.I. Moura, A.M. Dias, E. Carvalho, et al., Acta Biomater. 9 (2013) 7093–7114.
[11] L. Chen, Y. Chen, R. Zhang, et al., ACS Nano 16 (2022) 9929–9937.
[12] C. Wang, L. Wang, V. Nallathambi, et al., Adv. Mater. 36 (2024) e2405200.
[13] Y. Li, R. Fu, Z. Duan, et al., Small 18 (2022) e2200165.
[14] X. Yang, M. Yang, B. Pang, et al., Chem. Rev. 115 (2015) 10410–10488.
[15] X. Zhao, L. Chang, Y. Hu, et al., ACS Appl. Mater. Interfaces 14 (2022) 18194–18208.
[16] S. Li, Y. Zhang, H. Jin, et al., J. Colloid Interf. Sci. 651 (2023) 319–333.
[17] T. Wang, Y. Li, Y. Liu, et al., J. Colloid Interf. Sci. 633 (2023) 851–865.
[18] J. Xu, J. Li, W. Zhong, et al., Chin. Chem. Lett. 32 (2021) 2390–2394.
[19] L. Wang, Q. Hou, W. Zheng, et al., ACS Nano 15 (2021) 17885–17894.
[20] Q. Li, F. Fu, M. Zhao, et al., Chin. Chem. Lett. 36 (2025) 110090.
[21] H. Deng, K. Huang, L. Xiu, et al., Nat. Commun. 13 (2022) 3381.
[22] K. Chen, G. Dai, S. Liu, et al., Chin. Chem. Lett. 34 (2023) 107638.
[23] D. Yang, Z. Li, Y. Lian, et al., Chin. Chem. Lett. 36 (2025) 109717.
[24] M. Zhou, T. Higaki, G. Hu, et al., Science 364 (2019) 279–282.
[25] K. Huang, H. Ma, J. Liu, et al., ACS Nano 6 (2012) 4483–4493.
[26] T. Wang, Y. Ju, Y. Cheng, et al., Chin. Chem. Lett. 36 (2025) 109871.
[27] Z. Luo, K. Zheng, J. Xie, Chem. Commun. 50 (2014) 5143–5155.
[28] Y. Wang, M.J. Malkmes, C. Jiang, et al., J. Hazard. Mater. 416 (2021) 126236.
[29] K. Zheng, M.I. Setyawati, T.P. Lim, et al., ACS Nano 10 (2016) 7934–7942.
[30] Q. Zheng, C. Chen, Y. Liu, et al., Int. J. Nanomed. 19 (2024) 965–992.
[31] Z. Ruan, C. Zhang, T. Shi, et al., Mater. Today Bio 16 (2022) 100426.
[32] Z. Wei, T. Xu, C. Wang, et al., Nanoscale 16 (2024) 10656–10662.
[33] S. Panicker, I.M. Ahmady, C. Han, et al., Mater. Today Chem. 16 (2020) 100237.
[34] S. Chen, K. Kimura, Langmuir 15 (1999) 1075–1082.
[35] N.E. Motl, E. Ewusi-Annan, I.T. Sines, et al., J. Phys. Chem. C 114 (2010) 19263–19269.
[36] B. Zhang, Z. Wu, Y. Cao, et al., J. Phys. Chem. C 125 (2021) 489–497.
[37] H. Yang, Y. Wang, J. Lei, et al., J. Am. Chem. Soc. 135 (2013) 9568–9571.
[38] Y. Song, Y. Lv, M. Zhou, et al., Nanoscale 10 (2018) 12093–12099.
[39] Y. Song, Y. Li, H. Li, et al., Nat. Commun. 11 (2020) 478.
[40] W. Wang, Y. Cui, X. Wei, et al., ACS Nano 18 (2024) 15845–15863.
[41] D. Dong, Z. Cheng, T. Wang, et al., Int. J. Biol. Macromol. 234 (2023) 123745.
[42] H. Chen, Y. Jiang, T. Xu, et al., J. Mater. Chem. B 10 (2022) 4789–4799.
[43] S.W. Kim, W.K. Lee, J.S. Lee, ACS Omega 8 (2023) 46267–46275.
[44] S. Zhang, L. Nguyen, J. Liang, et al., Nat. Commun. 6 (2015) 7938.
[45] C. Ling, X. Liu, H. Li, et al., Angew. Chem. Int. Ed. 61 (2022) e202200670.
[46] J. Muri, M. Kopf, Nat. Rev. Immunol. 21 (2021) 363–381.
[47] B. Kalyanaraman, Redox Biol. 1 (2013) 244–257.
[48] H. Su, J. Huang, S. Weng, et al., Redox Biol. 48 (2021) 102206.
[49] B. Zhu, J. Wu, T. Li, et al., Adv. Healthc. Mater. 13 (2024) e2302485.
[50] J. Wu, Y. Yu, Y. Cheng, et al., Angew. Chem. Int. Ed. 60 (2021) 1227–1234.
[51] W. Zhang, T. Xu, Y. Chen, et al., Polyoxometalates 4 (2025) 9140082.
[52] K. Feng, G. Wang, S. Wang, et al., Adv. Mater. 36 (2024) e2401619.
[53] S. Zhang, F. Ding, Y. Liu, et al., Carbohydr. Polym. 292 (2022) 119615.
[54] G. Liu, Y. Zhou, Z. Xu, et al., Chin. Chem. Lett. 34 (2023) 107705.
[55] Y. Sun, Y. Zhu, J. Si, et al., Chin. Chem. Lett. 36 (2025) 110012.
[56] Y. Zhang, Z.L. Wang, Z.P. Deng, et al., Carbohydr. Polym. 315 (2023) 120973.
[57] D. Huang, J. Du, F. Luo, et al., Adv. Healthc. Mater. 13 (2024) e2303379.
[58] H. Li, F. Cheng, X. Wei, et al., Mater. Sci. Eng. C: Mater. Biol. Appl. 118 (2021) 111324.
[59] J. Dong, S. Zhang, Y.K. Chan, et al., Biomaterials 320 (2025) 123258.
[60] H. Ma, Y. Luo, Y. Wang, et al., Bioact. Mater. 49 (2025) 531–548.
[61] C. Liu, L. Guo, P. Yue, et al., J. Control. Release 381 (2025) 113627.
[62] S. Pourshahrestani, E. Zeimaran, N.A. Kadri, et al., Adv. Healthc. Mater. 9 (2020) e2000905.
[63] Z. Wang, Z. Sun, S. Zhu, et al., Bioact. Mater. 50 (2025) 30–46.
[64] Y. Liao, Z. Zhang, W. Hu, et al., Biomaterials 318 (2025) 123182.
[65] X. Liang, H. Chen, R. Zhang, et al., Biomaterials 317 (2025) 123076.
[66] P. Ye, Y. Yang, M. Liu, et al., Adv. Mater. 37 (2025) e2419430.
[67] F. Dai, J. Zhang, F. Chen, et al., Adv. Sci. 11 (2024) e2408783.
[68] H. Xu, Y. Li, J. Song, L. Zhou, et al., Bioact. Mater. 35 (2024) 31–44.
[69] M. Eisenstein, Nature 588 (2020) 210–211.
[70] G. Wang, Z. Lin, Y. Li, et al., Adv. Drug. Deliv. Rev. 194 (2023) 114727.
[71] S. Balasubramanian, J. Skaf, U. Holzgrabe, et al., Front. Microbiol. 9 (2018) 1473.
[72] E.S. Lee, E.Y. Lee, J. Yoon, et al., Mar. Drugs 18 (2020) 463.
[73] X. Yang, T. Che, S. Tian, et al., Adv. Healthc. Mater. 13 (2024) e2400856.
[74] C. Hemsley, S. Abraham, S. Rowland-Jones, Clin. Infect. Dis. 29 (1999) 938–939.
[75] M. Miyamoto, R. Tsuboi, K. Harada, et al., J. Dermatol. 48 (2021) 1106–1108.
[76] E. Virgilio, M. Solmone, A. Scardigno, et al., J. Wound Care 32 (2023) 811–820.
[77] Y. Zheng, R.L. Hunt, A.E. Villaruz, et al., Cell Host Microbe 30 (2022) 301–313.
[78] M.M. Severn, A.R. Horswill, Nat. Rev. Microbiol. 21 (2023) 97–111.